THE JOURNAL OF PHYSICAL CHEMISTRY C

ARTICLE

pubs.acs.org/JPCC

Nanoengineered PtCo and PtNi Catalysts for Oxygen Reduction Reaction: An Assessment of the Structural and Electrocatalytic Properties

Rameshwori Loukrakpam,[†] Jin Luo,[†] Ting He,[‡,∥] Yongsheng Chen,[§] Zhichuan Xu,[†] Peter N. Njoki,[†] Bridgid N. Wanjala,[†] Bin Fang,[†] Derrick Mott,[†] Jun Yin,[†] Jonathan Klar,[†] Brian Powell,[†] and Chuan-Jian Zhong*[,†]

[†]Department of Chemistry, State University of New York at Binghamton, Binghamton, New York 13902, United States

[‡]Honda Research Institute, Columbus, Ohio 43212, United States

[§]EMS Energy Institute and Department of Energy and Mineral Engineering, The Pennsylvania State University, 155 Hosler Building, University Park, Pennsylvania 16802, United States

Supporting Information

ABSTRACT: The ability to nanoengineer catalysts in terms of size, composition, shape, and phase properties is essential in exploiting the catalytic properties. This paper reports the results of an investigation of the structural and electrocatalytic properties of PtM (M = Co and Ni) nanoparticles and their carbon-supported electrocatalysts for an oxygen reduction reaction (ORR). Examples are focused on PtCo and PtNi nanoparticles in the range of 2−9 nm and in the composition range of 50−75% Pt. A sharp contrast in size dependence of the activity was revealed between PtCo/C and PtNi/C catalysts, showing a clear trend of decrease in activity with increasing particle size for PtCo/C and a subtle increase in activity for PtNi/C. The size−activity correlation also depends on the bimetallic composition. The detailed analyses of the structures of the catalysts by XAS technique revealed important information for assessing the electrocatalytic properties in relation to the relative amount of oxygenated species and the relative change in interatomic bond distance in the bimetallic nanoparticles, which suggest that a combination of structural parameters such as the change in Pt−Pt bond distance, the segregation of metal phases, and the formation of surface oxygenated species is operative for the size dependence of the enhanced electrocatalytic activity.

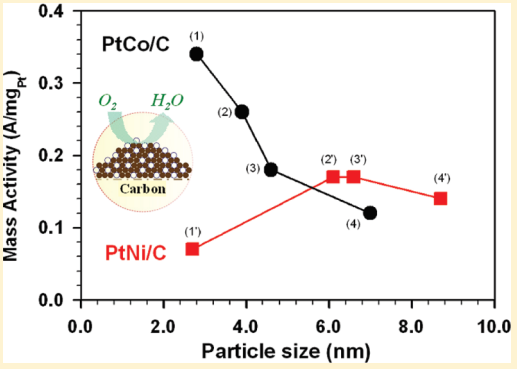

INTRODUCTION

The Proton Exchange Membrane Fuel Cell (PEMFC) represents one of the most effective ways of hydrogen utilization because of its high conversion efficiency, low pollution, light weight, and high power density for a wide range of applications such as power sources in automobiles, space shuttles, buildings, and factories. The Pt-based catalyst is currently one of the key components in fuel cells, which accounts for ∼30% of the cost of fuel cell manufacturing.[1] A key challenge to the ultimate commercialization of fuel cells is the development of active, robust, and low-cost catalysts for an oxygen reduction reaction (ORR).[2−5] There is a significant kinetic limitation for oxygen reduction at the cathode of PEMFCs operating at low temperature (<100 °C). The durability of Pt-based catalysts in fuel cells can also be compromised by sintering and dissolution. In addition, the propensity of poisoning by adsorbed reaction intermediate species poses a major problem to the sustenance of high catalytic activity of Pt-based catalysts.[6−9] There has been increasing interest in developing Pt-alloy or alternative catalysts that are low cost, active, and stable,[10,11] which is also driven by the high cost and the limited global supply of platinum.[12] The design of multimetallic alloy catalysts stems from exploring the synergistic properties as a result of the change in the surface binding sites, the lattice changes, and the electronic effects for enhancing the catalytic activity, improving the stability, and reducing the use of Pt. The rate of breaking the O═O bond to form water strongly depends on the degree of its interaction with the adsorption sites of the catalyst and the kinetics of electron transfer. Recent work on the cathode electrocatalysts has focused on understanding the mechanism of oxygen reduction on Pt-based bimetallic catalysts such as Pt−Fe, Pt−Ni, Pt−Cr, Pt−Cu, Pt−Au, and Pt−Co, etc.[13−20] The enhanced catalytic activities have been attributed to a number of factors including lattice shrinking or lattice strain due to the change in Pt−Pt bond

Received: October 7, 2010
Revised: December 13, 2010
Published: January 5, 2011

distance, d-band center shift, and a Pt skin effect as a result of thermal or acid treatments.

Catalysts of Pt alloyed with Co or Ni have attracted widespread interest in recent years.[21,22] For example, the near-surface chemical compositions were recently shown to influence the ORR activity of Pt_3Co catalysts.[23] The enhanced electrocatalytic activity of acid-treated catalysts was attributed to the formation of percolated Pt-rich and Pt-poor regions within individual Pt_3Co nanoparticles. High-temperature annealing of the acid-treated Pt_3Co was shown to promote ordering of Pt and Co and induce Pt segregation on the (100) surface in the first two to three surface layers for ordered Pt_3Co nanoparticles. In a study of ordered and disordered alloy phases of Pt_3Co electrocatalysts,[24] it is revealed that Pt_3Co annealed at 600 °C forms multiple phases, including (i) a disordered face-centered cubic (fcc) $Pt_{95}Co_5$ phase and (ii) an ordered face-centered tetragonal (L10) $Pt_{50}Co_{50}$ phase. By annealing at a higher temperature (950 °C), a single ordered primitive cubic (L12) Pt_3Co phase is formed. The ordered alloy phases in both catalysts were not stable under electrochemical treatment, exhibiting corrosion and dissolution or phase transformation into a disordered structure. The PtCo alloy catalyst (60−80 at % Co) in prevalence of a Co-rich disordered "fcc2" phase is found to exhibit the largest activity gain for ORR.[25] The Pt-rich alloy (fcc1) and ordered fct phase were found to diminish the activity gain. $PtCo_3$/C catalysts treated between 350 and 1000 °C under reductive conditions were recently shown to exhibit partial oxidative leaching of cobalt and a subsequent mass activity increase.[26] The leaching of Co from PtCo alloy catalysts in acidic conditions has also been shown to affect the long-term durability of the catalysts significantly.[27] The ORR activity of Pt_3Co is also recently demonstrated to be size dependent, exhibiting an initial increase with the particle size with a maximum mass activity around 4.5 nm.[28,29] The size dependence was believed to reflect a balance of the average coordination number and the surface Co leaching of the catalysts. In another study,[30] the PtCo/C catalyst treated at 500 °C with an average of 4.5 nm was found to exhibit the highest activity for ORR. In several studies of activity and durability,[31,32] PtCo/C catalysts were shown to exhibit a higher activity for ORR than Pt/C, but the loss in activity was higher than Pt/C. The lower stability of the PtCo catalyst during repetitive potential cycling was attributed to dissolution and redeposition of Pt, forming a surface layer of nonalloyed pure Pt. The presence of nonalloyed Co and its oxides on the catalyst surface following the thermal treatment was believed to hinder the reach of molecular oxygen to the Pt sites, leading to a lower activity.

For PtNi catalysts, surface segregation of metals was found to result in a pure Pt surface atomic layer.[33] The Ni-rich subsurface atomic layer was believed to determine the electronic properties of the surface, leading to a reduced coverage of adsorbing species, hydrogen and OH, on the $Pt_3Ni(111)$ compared to the pure Pt(111) electrode. The contraction of the Pt_3Ni surface during the adsorption of OH appears to stabilize the surface over a wider potential range than pure Pt as it inhibits irreversible roughening due to oxide formation. The understanding of the stability and atomic structure of the $Pt_3Ni(111)$ surface is thus believed to be important in probing the origin of its increased activity for ORR.[33] Pt_3Ni with controlled shapes in the 3−11 nm size range was recently shown to exhibit a {111}/{100} activity ratio of 4−5 for ORR.[34,35] The understanding of the effect of crystal planes/faces on the activity of Pt and Pt-based catalysts remains unclear due to the lack of ability to control the facet sizes and defects in the facets. Either the Pt(111) face on the surface of Pt/Pt-based alloy particles[36,37] or the (100) face has been considered[38,39] to be responsible for the increased activity. In our recent comparison of Pt-nanocube and Pt-nanoparticle catalysts under similar size ranges, the (100) faces on the Pt-nanocubes/C were considered to be at least partially responsible for the increase in the specific activity for ORR.[39]

Theoretical studies (e.g., density function theory) of Pt_3X (X = Fe, Co, Ni) bulk alloys for ORR have also revealed some insights for the understanding of the Pt surface properties. In the study by Norskov et al., the Pt skins were found to be stabilized over Pt.[40] The alloys were shown to occur only on the surface layers which were predicted to be active for ORR but thermodynamically unstable.[41] In the theoretical study of the adsorption of atomic oxygen on Pt-segregated and nonsegregated surfaces of $Pt_3M(111)$ (M = Fe, Co, and Ni),[42] the surface adsorption properties were found to be considerably modified by introducing 3d metals. For each alloy system, the binding strength of oxygen followed the order of Pt-skin < Pt(111) < Pt_3M. Among the three alloys, $Pt_3Fe(111)$ was the most favorable for oxygen adsorption on the nonsegregated surface, whereas $Pt_3Ni(111)$ was preferred on the Pt-segregated surface. The magnitude of surface adsorption energies was determined by both the surface geometry and the electronic structure. The electronic structure of the surface Pt atoms only differs very slightly for the segregated and nonsegregated alloys. The discrepant adsorption properties are therefore mainly attributed to the direct involvement of 3d metals either on the surface or in the subsurface. The electrochemical stability of the alloys in the presence of adsorbed oxygen indicated an enhanced electrochemical stability of Pt-skin surfaces produced from Pt_3M alloys. While oxygen adsorption is found to destabilize both the Pt-skin and pure Pt surfaces, the Pt-skin surfaces under adsorbed oxygen are still more stable against dissolution than the pure Pt surfaces under the same oxygen coverage.

Despite these extensive experimental and theoretical studies, the understanding of the correlation between the electrocatalytic activity and the nanostructural parameters (e.g., size and composition) remains elusive. In this report, we describe the results of an investigation of the structural and electrocatalytic properties of PtM (M = Co and Ni) nanoparticles and their carbon-supported electrocatalysts for oxygen reduction reaction (ORR), focusing on the comparison of the different results between PtCo and Pt catalysts. The PtCo/C and PtNi/C catalysts were prepared by assembly of as-synthesized PtCo and PtNi nanoparticles (in the range of 1−10 nm and the bimetallic compositions of $Pt_{75}M_{25}$ and $Pt_{50}M_{50}$) on carbon support, respectively, followed by thermal treatment. Note that the bimetallic compositions of our catalysts were determined by spectroscopic methods, in contrast to some of the literature reports where the bimetallic composition was often directly taken from the feeding ratio of metal precursors used in the synthesis which could introduce uncertainties in data analysis. The structure and morphology of the catalysts were characterized using XRD and XAS techniques, and were used for establishing the correlation between the electrocatalytic ORR activity and the catalyst size and composition.

EXPERIMENTAL SECTION

Chemicals. Platinum(II) acetylacetonate ($Pt(acac)_2$, 97%), cobalt(II) acetylacetonate ($Co(acac)_2$, 97%), cobalt carbonyl

($Co_2(CO)_8$), nickel(II) acetylacetonate ($Ni(acac)_2$, 97%), 1,2-hexadecanediol (90%), octyl ether (99%), oleylamine (70%), and oleic acid (99+%) were purchased from Aldrich and used as received. Other chemicals such as ethanol and hexane were purchased from Fisher Scientific.

Nanoparticle Synthesis. The composition of the $Pt^0_{n1}M^0_{n2}$ (M = Co or Ni) nanoparticles, where $n1$ and $n2$ represent the atomic percentages of each metal, was controlled by the feeding ratio of the metal precursors such as platinum(II) acetylacetonate and cobalt carbonyl or nickel(II) acetylacetonate which are expressed in molar percentages.

PtCo Nanoparticles. The general synthesis of PtCo nanoparticles involved the use of three metal precursors, $Pt(acac)_2$ and $Co_2(CO)_8$ (or $Co(acac)_2$), in controlled molar ratios. These metal precursors were dissolved in an octyl ether solvent. A mixture of oleylamine and oleic acid was also dissolved in the solution and used as capping agents. 1,2-Hexadecanediol was used as a reducing agent for the reduction of the Pt precursor, and elevated temperature was used to initiate the thermal decomposition of the Co precursor. The general reaction for the synthesis of the (oleylamine/oleic acid)-capped PtCo nanoparticles thus involved a combination of thermal decomposition and reduction reaction. $Pt(acac)_2$ is reduced to Pt^0 by 1,2-hexadecanediol, whereas $Co_2(CO)_8$ is thermally decomposed into Co^0.

In a typical procedure for the synthesis of 2 nm sized $Pt_{75}Co_{25}$, for example, 543 mg of 1,2-hexadecanediol (1.89 mmol), 275 mg of platinum acetylacetonate Pt(acac)2 (0.68 mmol), and 60 mL of octyl ether (or benzyl ether) were added to a three-neck 250 mL flask under stirring. The solution was purged with N_2 and heated to 105 °C. The solution was a dark green color. At this temperature and under N_2 atmosphere, 0.5 mL of oleylamine (1.06 mmol), 0.5 mL of oleic acid (1.56 mmol), and 103 mg of $Co_2(CO)_8$ (0.30 mmol in 3 mL of octyl ether) were added into the solution. N_2 purging was stopped, and the solution was kept under N_2. The mixture was heated to 270 °C and refluxed for 30 min. The solution was a black color. After the reaction mixture was allowed to cool to room temperature, the solution was transferred to a large flask under ambient environment. The nanoparticle product was soluble in the reaction solution. The product was precipitated by adding ethanol (~300 mL). The yellow-brown supernatant was discarded. The black precipitate was dried under N_2 and was redispersed in hexane and stored under N_2. The protocol for the synthesis of 5 nm PtCo nanoparticles was similar to that for the 2 nm PtCo nanoparticles but with slight modifications in the amounts of 1,2-hexadecanediol, oleylamine, and oleic acid and the reflux time.

PtNi Nanoparticles. We have succeeded in synthesizing PtNi nanoparticles in the size range of 2−10 nm. In a typical synthesis of 2 nm PtNi nanoparticles, super hydrate (lithium triethylborohydride) was used as the reducing agent. Briefly, 1 mL of oleylamine, 1 mL of oleic acid, $Pt(acac)_2$, and $Ni(acac)_2$ were added into a 250 mL three-neck flask containing 20 mL of benzyl ether under stirring. The solution is purged with N_2 and heated to 100 °C and then injected with 12 mL of super hydrate. The solution changed color to dark and was maintained at 100 °C for 20 min. After the reaction mixture was allowed to cool to room temperature, the solution was transferred into a large flask under ambient environment. The following process was the same as PtCo nanoparticle synthesis. This modification of the reducing agent was aimed at creating a condition with a greater reducing power for the formation of smaller-sized PtNi nanoparticles. For the synthesis of 5 nm PtNi nanoparticles, 543 mg of 1,2-hexadecanediol (2.1 mmol), 0.3−0.7 mmol of $Pt(acac)_2$, 0.3−0.7 mmol of $Ni(acac)_2$, 2 mL of oleylamine (5.4 mmol), and 2 mL of oleic acid (6.2 mmol) were added to a three-neck 250 mL flask with 60 mL of octyl ether under stirring. The solution is purged with N_2 and heated to 100 °C and then heated to 270 °C for 30 min.

In general, the basic protocol for the synthesis of both PtCo and PtNi nanoparticles followed our earlier reports on other bimetallic and trimetallic nanoparticles[43−45] by establishing the correlation curves in terms of composition or size vs feeding and reaction conditions (see Figure S3 in Supporting Information for the experimental correlation curves for both PtCo and PtNi nanoparticles in terms of the controllability over composition).

Preparation of PtCo/C and PtNi/C Catalysts. The typical preparation procedure of the carbon-supported PtCo nanoparticles included the following steps. The loading of the metal nanoparticles on the carbon support was controlled by their feeding ratios at either 20 or 40%. First, 320 mg of carbon black (ECP, Ketjen Black International, Tokyo) was suspended in 300 mL of hexane. After sonicating for ~3 h, 80 mg of PtCo ($Pt_{75}Co_{25}$) was added into the suspension (for 20% loading). The suspension was sonicated for 30 min, followed by stirring for ~15 h. The suspension was evaporated slowly for 4−8 h by purging N_2 while stirring. The powder was collected and dried under N_2. The thermal treatment involves removal of organic shells and calcination of the alloy nanoparticles. All samples were treated in a tube furnace using a quartz tube. The assembled PtCo/C samples were first heated at 260 °C in 20% O_2/80% N_2 for 90 min for removing the organic shells and then heated at 400 °C in 7% H_2/93% N_2 for 120 min for calcination. The loading of the PtCo/C catalysts after calcination was determined using TGA.

Measurements and Instrumentation. The following techniques were used for the characterization of the nanoparticles and catalysts.

Transmission Electron Microscopy. Transmission electron microscopy (TEM) was performed on a Hitachi H-7000 electron microscope (100 kV) and FEI Tecnai T12 Spirit Twin TEM/SEM electron microscope (120 kV). For TEM measurements, the catalyst samples were suspended in hexane solution and were drop cast onto a carbon-coated copper grid followed by solvent evaporation in air at room temperature.

High-Resolution Transmission Electron Microscopy−Electron Diffraction X-ray Spectroscopy. High-Resolution Transmission Electron Microscopy−Electron Diffraction X-ray Spectroscopy (HRTEM−EDX) was carried out using a JEOL JEM 2010F with an acceleration voltage of 200 kV and a routine point to point resolution of 0.194 nm.

Direct Current Plasma−Atomic Emission Spectroscopy. The composition was analyzed using the direct current plasma−atomic emission spectroscopy, which was performed using an ARL Fisons SS-7 Direct Current Plasma−Atomic Emission Spectrometer (DCP−AES). Measurements were made on emission peaks at 265.95, 259.94, and 231.60 nm for Pt, Co, and Ni, respectively. The nanoparticle samples were dissolved in concentrated aqua regia and then diluted to concentrations in the range of 1−50 ppm for analysis. Calibration curves were made from dissolved standards with concentrations from 0 to 50 ppm in the same acid matrix as the unknowns. Detection limits, based on three standard deviations of the background intensity, are 0.02, 0.002, and 0.005 ppm for Pt, Co, and Ni. Standards and unknowns were analyzed 10 times each for 3 s counts. Instrument reproducibility, for concentrations

greater than 100 times the detection limit, is less than ±2% error. The metal composition was expressed as $Pt_{n1}M_{n2}$ (M = Co or Ni), where $n1$ and $n2$ represent the atomic percentage of the element in the ternary catalyst.

Thermogravimetric Analysis. Thermogravimetric analysis (TGA) was performed on a Perkin-Elmer Pyris 1-TGA for determining the metal loading on carbon black. Typical samples weighed ~4 mg and were heated in a platinum pan. Samples were heated in 20% O_2 at a rate of 10 °C/min.

X-ray Powder Diffraction (XRD). The thermally treated catalysts were examined by powder X-ray diffraction. Powder diffraction patterns were recorded on a scintag XDS 2000 $\theta-\theta$ powder diffractometer equipped with a Ge(Li) solid state detector (Cu Kα radiation). The data were collected from 10° to 90° 2θ at a scan rate of 0.02° 2θ per step and 30 s per point.

X-ray Absorption Fine Structure (XAFS) Spectroscopy. Pt L3 edge (11 564 eV), Ni K edge (8333 eV), and Co K edge (7709 eV) XAFS spectra were collected on the insertion device beamline of the Materials Research Collaborative Access Team (MRCAT) at the Advanced Photon Source, Argonne National Laboratory. A cryogenic double-crystal Si(111) monochromator was used along with a Rh-coated mirror to reduce harmonics. All spectra were collected in transmission mode. Powder samples were pressed into pellets with proper thickness to ensure that the absorption edge height, $\Delta\mu x$, was below 1.5 to eliminate leakage effects and yet not too small to provide a good signal/noise ratio. X-ray intensity before and after sample was measured by ionization chambers filled with N_2. In addition, a reference spectrum of Pt, Ni, or Co foil for energy calibration was collected simultaneously with each scan using an additional ionization chamber.

Practically, XAFS can be divided into two regions, the near-edge region and extended region. The near-edge XAFS, or X-ray absorption near-edge structure (XANES), provides information on oxidation state and coordination symmetry and can be used for identification of different species by fingerprinting. In contrast, extended XAFS, or EXAFS, measures the coordination structure including bond distance and coordination number of neighboring atoms. A detailed description of XANES and EXAFS theory and data processing was provided elsewhere.[46] XANES spectra were processed using Athena.[47] EXAFS spectra were extracted using Athena, and fitting of EXAFS data was performed using Artemis.[47] Background removal and edge-step normalization were performed using the AUTOBK program.[47] FEFFIT[48] was then used to fit the EXAFS function using paths for Ni or Pt species (Ni−O, Ni−Pt, Ni−Ni, Pt−O, Pt−Ni, Pt−Pt, etc.) as generated by the FEFF code (version 6.0).[49] The fitting was limited to a k range of 2.0−13.0 $Å^{-1}$ for Ni K edge spectra and 2.0−16.0 $Å^{-1}$ for Pt L3 edge spectra, using a Hanning window with dk = 1.0 $Å^{-1}$. The fits were performed to both the real and imaginary parts of $\chi(R)$ in the region of $1.0 < R < 3.2$ Å. A similar analysis was performed on reference samples of Ni and Pt foils to obtain S_0^2, the amplitude reduction factor, for the subsequent determination of the coordination numbers of the fitted structure of the samples.

Electrochemical Activity. The electrochemical activity for oxygen reduction was measured using the hydrodynamic rotating disk electrode technique. The standard three-electrode configuration was used with Pt wire as the counter electrode and RHE as the reference electrode. A glassy carbon-based working electrode with a geometric surface area of 0.196 cm^2 was used, and 15 μL of catalyst ink was pipetted and uniformly distributed over the glassy carbon surface. To prepare catalyst ink, 5 mg of supported catalysts was mixed with 4 mL of Milli-Q water and 1 mL of isopropanol and 20 μL of Nafion solution (5 wt %, Aldrich). The solution was ultrasonicated using a pulse ultrasonic probe for 10 min at 20% amplitude to form uniform ink. The cyclic voltammetry (CV) was performed in saturated N_2 0.5 M H_2SO_4 at room temperature to clean the catalyst surface. Optima grade sulfuric acid (Fisher Scientific) diluted with Milli-Q water to 0.5 M H_2SO_4 was used as electrolyte, and it was deaerated with high-purity nitrogen before the measurement. The rotating disk electrode (RDE) measurements were performed using a Pine Instrument. Before the measurement, the sulfuric acid was saturated with pure oxygen. All RDE measurements were performed under the rotating speed of 2000 rpm and 5 mV/s scan rate. All potentials were reported with respect to the RHE reference electrode. The activity measurements were reproducible with less than 10% standard deviation. CV and RDE curves were recorded after multiple cycles (≥8 cycles) in the potential window of 0.0−1.2 V which was shown to establish a stabilized current. Mass-specific activity was used throughout the report for data comparison

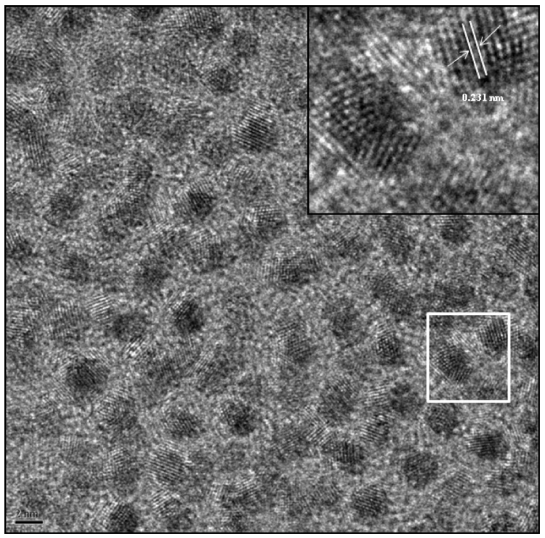

Figure 1. HRTEM for as-synthesized PtCo nanoparticles ($Pt_{73}Co_{27}$, 1.8 ± 0.4 nm) (scale bar = 2 nm). Inset image: a magnified view of the nanoparticles from the box-indicated area.

RESULTS AND DISCUSSION

1. Size, Composition, and Morphology of PtCo, PtNi, PtCo/C, and PtNi/C. PtCo nanoparticles were obtained with different average sizes, ranging from 1 to 8 nm, e.g., $Pt_{73}Co_{27}$ (1.8 ± 0.4 nm) and $Pt_{70}Co_{30}$ (6.7 ± 0.7 nm). The observed nanoparticles are largely characterized by the highly faceted nanocrystal feature, which is observable by a close examination of the shapes of the individual nanocrystals. On the basis of TEM data, the particle sizes are very well controlled, and the size monodispersity is very high. The fact that the nanoparticles have well-defined interparticle spacing and display domains of hexagonal ordering is indicative of the encapsulation of the nanocrystal cores by organic monolayers. These nanoparticles exhibit relatively high monodispersity (average standard deviation: 0.3−0.7 nm).

Figure 1 shows HRTEM data for a sample of $Pt_{73}Co_{27}$ nanoparticles. The particles display highly crystalline feature with multiple facets. The HRTEM−EDS analysis of small

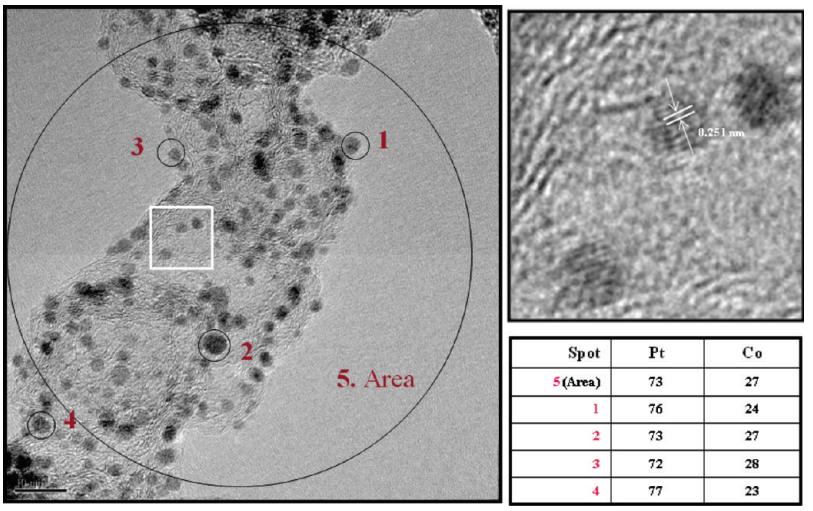

Spot	Pt	Co
5(Area)	73	27
1	76	24
2	73	27
3	72	28
4	77	23

Figure 2. HRTEM−EDX data for the $Pt_{73}Co_{27}/C$ catalyst (scale bar = 10 nm). Right top: a magnified view of the nanoparticles from the box-indicated area showing a lattice fringe of 0.251 nm. Right bottom: EDX data showing the composition of four different-sized nanoparticles and the area.

domains in the observed nanoparticles revealed a composition of $Pt_{70}Co_{30}$, which is very close to the composition determined by DCP-based bulk analysis data ($Pt_{73}Co_{27}$). With both DCP and EDX data, we believe that the composition value reflects the bimetallic composition at the individual particle level. The PtCo nanoparticles were analyzed using DCP−AES and ICP−MS techniques to determine the relative metal compositions in the nanoparticles as a function of synthetic feed ratios in octyl ether. In general, the data showed that the relative composition of Pt in the nanoparticle product scales approximately linearly with the feed composition in the synthetic reaction solution for both solvents. The size of PtCo nanoparticles is controlled by two factors. One is the precursor concentration, and the other is the capping agent concentration. At a high precursor concentration, the nanoparticles grow into larger-sized particles. Reduction of the amount of capping agent in the solution results in insufficient capping of nanoparticles, which allows more precursor atoms to reach the nanoparticle surface, favoring the growth process.

Similarly, PtNi nanoparticles were obtained with different average sizes, ranging from 1 to 10 nm, e.g., $Pt_{78}Ni_{22}$ (1.5 ± 0.3 nm) and $Pt_{71}Ni_{29}$ (5.0 ± 0.8 nm). The correlation between the feeding molar ratio and the product molar ratio for both PtCo and PtNi nanoparticles was found to be largely linear (see Figure S3 in Supporting Information), demonstrating good controllability over composition by controlling the feeding ratio. Similar to PtCo nanoparticles, the particle size and monodispersity for PtNi nanoparticles were also found to be controllable by manipulating the metal feeding ratio and reaction conditions (temperature and solvent), as shown in our earlier reports on other bimetallic and trimetallic nanoparticles.[44,45]

For PtCo nanoparticles on carbon support materials, which were controlled by quantitative mixing in a solution of carbon suspension, TEM analysis of the PtCo nanoparticles supported on carbon, typically with a loading of 20−40%, showed basically unaffected particle sizes and relatively good dispersion. The thermal treatments of PtCo/C catalysts involved removal of organic shells and calcination of the binary nanoparticles. The development of effective thermal processing protocols for preparing PtCo/C catalysts is an important area of our investigation for ensuring the removal of the capping materials and the calcinations of the alloy properties. Although experimentally the loading was controlled by feeding at either 20 or 40%, we tried to ensure the actual loading by using TGA to determine the loading, which was found to range from 20 to 25% for the 20% feeding and 35 to 45% for the 40% feeding. Also, experimentally the composition was mostly kept the same (e.g., $Pt_{75}Co_{25}$) by feeding control; we tried to ensure the actual composition by using DCP−AES to determine the actual composition, which was found to display a deviation from the feeding control by 5−10% depending on the actual catalyst.

To find out the optimized thermal treatment condition, TGA experiments were carried out under various conditions. Under O_2 environment for the thermal treatment, the severe burning of the PtCo/C catalysts at a relatively low temperature was found to be a major problem. After examining a series of N_2−O_2 treatment conditions, we believe that we have discovered a new and promising condition for the processing of PtCo/C catalysts. TGA data showed that the removal of the organic shell begins at 150 °C in both N_2 and 20% O_2 environment. However, burning of the carbon was evident at 185 °C under 20% O_2 environment. It is remarkable that the organic shell could be removed by thermal treatment under N_2 environment. We note that the temperature range for the removal of the organic shells and the burning was quite different from what we observed previously with PtNiFe/C or PtVFe/C catalysts.[44] To develop a better understanding of the effect of the thermal treatment conditions on the structural and catalytic properties, we examined a number of thermal treatment conditions for different PtCo/C samples.

For the thermally treated $Pt_{73}Co_{27}/C$, TEM analysis showed an average particle size of 2.8 ± 0.4 nm. For the sample treated under 20% O_2, the particle size showed an increase (from ~2 to ~6 nm), which is believed to be a result of burning. In addition to oxidation of carbon support, there was a certain degree of sintering of the particles as a result of the carbon burning. In some cases, the burning effect was so severe that the final product yielded a 45% loading. In contrast, only a slight increase in size was observed for the sample treated under N_2. For example, for sample $Pt_{73}Co_{27}/C$ there was a slight increase in size (from 1.8 to 2.8 nm) after the thermal treatment. For $Pt_{79}Co_{21}/C$ (~4.5 nm)/C, the size showed a small change which is within the standard deviation.

Figure 2 shows a set of HRTEM−EDX data for a sample of the $Pt_{73}Co_{27}/C$ catalyst. To address the question whether the

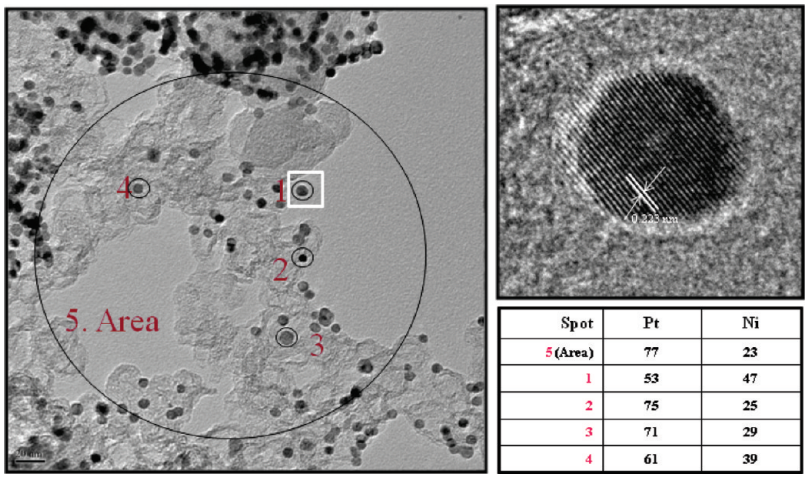

Spot	Pt	Ni
5 (Area)	77	23
1	53	47
2	75	25
3	71	29
4	61	39

Figure 3. HRTEM−EDX data for the $Pt_{71}Ni_{29}/C$ catalyst (scale bar = 20 nm). Right top: a magnified view of the nanoparticle from the box-indicated area showing a lattice fringe of 0.223 nm. Right bottom: EDX data showing the composition of four different-sized nanoparticles and the area.

nanoparticles are bimetallic in individual nanoparticles or in an ensemble of the nanoparticles, we analyzed both the composition of different areas in the TEM image and the composition-selected small- and large-sized individual nanoparticles. As shown by EDX data, the atomic compositions were found to be almost identical, independent of the particle sizes (2−9 nm). This finding is in contrast to the results often observed for bimetallic or trimetallic catalysts prepared from the traditional methods (e.g., coprecipitation) where large-sized particles are usually base metal rich whereas small particles are Pt rich.[44c]

Similar to the thermal treatment for PtCo/C catalysts, the thermal treatment parameters were also investigated using the TGA method to find the optimized thermal treatment condition for PtNi/C catalysts. Under O_2 environment, the burning of the PtNi/C catalysts at a relatively low temperature was found to be somewhat similar to that for PtCo/C catalysts. It shows that the removal of the organic shell begins at 150 °C in both N_2 and 20% O_2 environment. On the basis of the data, the PtNi/C catalysts were treated at 260 °C for 60 min in nitrogen environment and then calcined at 400 °C in 15% H_2 + 85% N_2 for 120 min. After thermal treatment, the metal loading was determined by TGA. On the basis of TEM and size distribution data for the thermally treated $Pt_{71}Ni_{29}/C$ catalyst, there is a slight increase in size (~1 nm) for the sample treated in comparison with the as-synthesized nanoparticles. Figure 3 shows HRTEM−EDX data for a sample of the thermally treated $Pt_{71}Ni_{29}/C$ catalyst. In addition to observing the highly crystalline feature of the particles, the atomic composition was found to be almost identical to the DCP-determined composition.

Table 1 summarizes the particle compositions, sizes, and loading data for a series of PtCo/C and PtNi/C catalysts. The original particle size was included in Table 1 to illustrate the change of the particle size after the thermal processing treatment of the catalysts. The feeding for all the catalyst loadings was controlled experimentally at either 20% or 40%, and the observed ±5% change in the actual loading is not unusual due to a burning effect.

2. X-ray Diffraction Analysis. The crystalline and lattice properties of the PtCo/C and PtNi/C catalysts were characterized using X-ray diffraction. Figure 4 shows a representative set of XRD patterns for several samples of PtCo/C and PtNi/C catalysts. Overall, the observed diffraction peaks can be indexed

Table 1. Summary of Particle Sizes and Lattice Constants for PtCo/C and PtNi/C Catalysts

catalysts	particle size NPs (nm)	particle size on carbon (nm)	metal loading (% wt)	lattice parameter (nm)	Scherer size (nm)
(A) PtCo/C					
$Pt_{73}Co_{27}/C$	1.8 ± 0.4	2.8 ± 0.4	37	0.3910	3.3
$Pt_{75}Co_{25}/C$	4.6 ± 0.4	4.6 ± 0.6	40	0.3904	3.8
$Pt_{52}Co_{48}/C$	2.5 ± 0.2	3.9 ± 0.7	24	0.3844	4.4
$Pt_{52}Co_{48}$NPs	2.5 ± 0.2	-	-	0.3903	1.8
$Pt_{70}Co_{30}/C$	6.7 ± 0.7	7.0 ± 0.7	36	0.3874	4.4
(B) PtNi/C					
$Pt_{71}Ni_{29}/C$	5.0 ± 0.8	6.6 ± 1.0	45	0.3920	4.9
$Pt_{78}Ni_{22}/C$	1.5 ± 0.3	2.7 ± 1.0	38	0.3895	1.7
$Pt_{64}Ni_{36}/C$	7.7 ± 2.3	8.7 ± 0.8	24	0.3890	7.3
$Pt_{56}Ni_{44}/C$	4.8 ± 0.5	6.1 ± 0.8	44	0.3817	3.6
$Pt_{64}Ni_{36}$ NPs	7.7 ± 2.3	-	-	0.3883	6.5

as (111), (200), (220), (311), and (222) reflections of fcc structure for all these samples. A close examination of the peak position reveals subtle differences in terms of lattice constants. In comparison with the database for single metal systems (e.g., 2θ values of 39.7 (111), 46.3 (200), and 67.3 (220) for Pt; 44.5 (111), 51.8 (200), and 76.3 (220) for Ni; and 44.3 (111), 51.6 (200), and 75.9 (220) for Co), it is observed that the diffraction peaks for the PtCo and PtNi catalysts are shifted to diffraction angles higher than those for Pt, indicating a reduction of the lattice constant. The replacement of a Pt atom by a Co/Ni atom with a smaller radius in the PtCo or PtNi alloy nanoparticles is believed to lead to the observed reduction of the lattice constant.

On the basis of the lattice constants derived from the XRD data for PtCo/C catalysts (Figure 4A, Table 1), the lattice constant for $Pt_{75}Co_{25}/C$ (4.6 ± 0.6 nm, (c)) was found to be slightly smaller than that for $Pt_{73}C0_{27}/C$ (2.8 ± 0.4 nm, (b)). This small difference reflects the similar composition (~Pt_3Co_1) for the two samples. Since the XRD peaks are significantly broadened for smaller-sized particles, it is difficult to assess the exact contribution of the decrease in particle size to the overall lattice reduction based on the XRD data. This assessment is

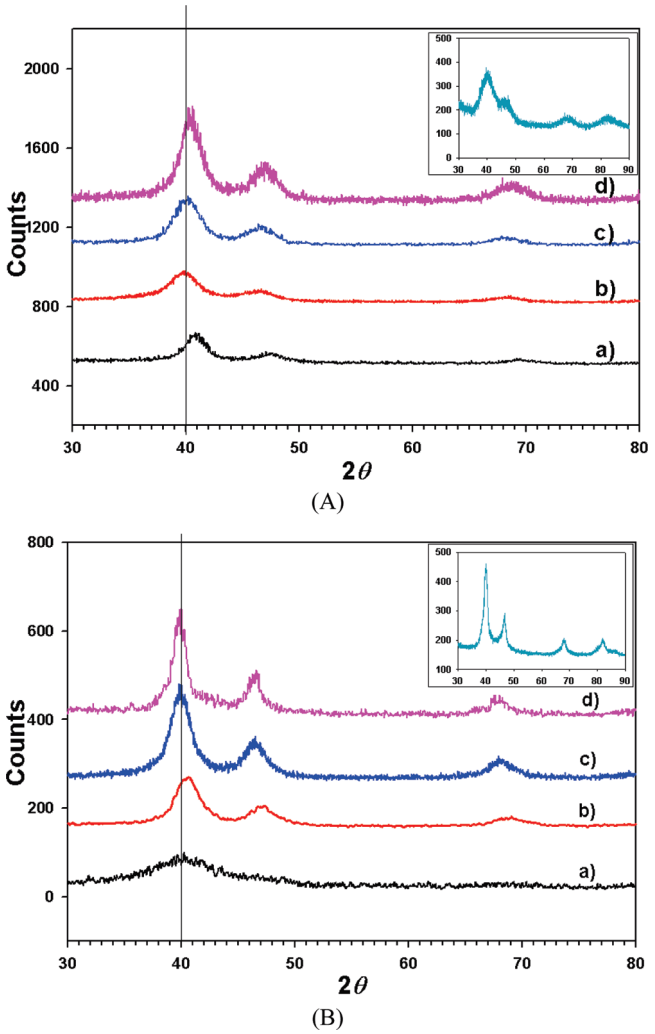

Figure 4. XRD patterns of (A) PtCo/C catalysts: (a) $Pt_{52}Co_{48}$/C (3.9 ± 0.7 nm), (b) $Pt_{73}Co_{27}$/C (2.8 ± 0.4 nm), (c) $Pt_{75}Co_{25}$/C (4.6 ± 0.6 nm), and (d) $Pt_{70}Co_{30}$/C (7.0 ± 0.7 nm); inset: $Pt_{52}Co_{48}$ /C before thermal treatment (2.5 ± 0.2 nm) and (B) PtNi/C catalysts: (a) $Pt_{78}Ni_{22}$/C (2.7 ± 1.0 nm), (b) $Pt_{56}Ni_{44}$/C (6.1 ± 0.8 nm), (c) $Pt_{71}Ni_{29}$/C (6.6 ± 1.0 nm), and (d) $Pt_{64}Ni_{36}$/C (8.7 ± 0.8 nm); and inset: as-synthesized $Pt_{64}Ni_{36}$ nanoparticles (7.7 ± 2.3 nm).

substantiated by comparison of data for catalysts with large difference in composition. For example, the lattice constant for $Pt_{52}Co_{48}$/C (3.9 ± 0.7 nm, (a)), 0.3844 nm, was found to be significantly smaller than that for the $Pt_{73}C0_{27}$/C (2.8 ± 0.4 nm, (b)) catalyst (0.3910 nm), though their particle sizes are similar. $Pt_{70}Co_{30}$/C (7.0 ± 0.7 nm, (d)) has a composition similar to $Pt_{73}Co_{27}$/C (2.8 ± 0.4 nm, (b)), but the larger particle size is shown to exhibit a smaller lattice constant (0.3874 nm). For PtCo, the as-synthesized particles ($Pt_{52}Co_{48}$/C before thermal treatment (2.5 ± 0.2 nm)) were very small (in contrast to the as-synthesized PtNi particles) and thus exhibited very broad XRD peaks, which made the reading of the peak position less precise in comparison with the calcined and thermally treated particles which showed a narrower peak width. The observed difference in the lattice parameter was partially due to the peak width effect, unlikely to reflect a significant difference in the actual lattice parameter.

By analysis of the lattice constants derived from the XRD data for PtNi/C catalysts (Figure 4B, Table 1), the lattice constant for $Pt_{71}Ni_{29}$/C (6.6 ± 1.0 nm, (c)) was also found to be slightly larger that that for the $Pt_{78}Ni_{22}$/C (2.7 ± 1.0 nm, (a)) catalyst. Similar to PtCo catalysts, the increase of Ni in the bimetallic nanoparticles was found to decrease the lattice constant, as evidenced by the comparison of the lattice constants for $Pt_{71}Ni_{29}$/C and $Pt_{78}Ni_{22}$/C (0.3920 and 0.3895 nm) with those for $Pt_{64}Ni_{36}$/C and $Pt_{56}Ni_{44}$/C (0.3890 and 0.3817 nm). For the catalysts with a feeding ratio controlled at $Pt_{75}Ni_{25}$, the 5−10% variation in the actual bimetallic composition was shown to have a relatively insignificant effect on the structural properties in comparison with the size effect. The observed lattice reduction can thus be attributed to the reduction in particle size.

In summary, the observed diffraction pattern indicates that the PtCo/C and PtNi/C catalysts prepared under the experimental condition are characteristic of alloy fcc structure. The lattice constant was found to decrease with the increase of base metals in the bimetallic alloy composition but to exhibit a less significant trend for the increase in particle size. While the particle sizes estimated from XRD are slightly higher than those determined from TEM data (Table 1), it is difficult to assess the exact contribution of the particle size to the overall lattice reduction by XRD data due to the significant peak broadening for the smaller-sized particles.

3. X-ray Absorption Fine Structure Spectroscopy. To gain further insight into the electronic structures of these catalysts, XAFS measurements were carried out with selected samples (e.g., $Pt_{64}Ni_{36}$/C (8.7 ± 0.8 nm) and $Pt_{52}Co_{48}$/C (3.9 ± 0.7 nm)). In Figure 5, a representative set of normalized XANES spectra are compared for these two catalysts, examining the details for the Pt L_3 edge for Pt and the Ni K edge for Ni in $Pt_{64}Ni_{36}$/C catalyst (a, b) and the Pt L_3 edge for Pt and the Co K edge for Co in $Pt_{52}Co_{48}$/C catalyst (c, d).

At the Pt L3 edge (Figure 5a and c), the white line (at around 11 567 eV) intensities of both catalysts are slightly higher than that of the Pt foil. These small changes indicated the decrease of 5d orbital filling in the Pt alloys due to oxidation and hybridization. At the Ni K edge (Figure 5b), the intensity of the pre-edge peak (at around 8335 eV) for $Pt_{64}Ni_{36}$/C decreases, while the white line (at around 8350 eV) intensity increases compared with the Ni foil. These changes demonstrated the strong hybridization between Pt and Ni and/or the formation of Ni oxides.[50,51] The same spectral characteristic is observed for the Co K edge XANES spectrum of $Pt_{52}Co_{48}$/C (Figure 5d). The white line (at around 7725 eV) intensity of the catalyst thermally treated at 400 °C is higher than that of the Co foil. For comparison, a spectrum of untreated catalyst (mainly Co oxide) is also included in Figure 5d, whose white line is found to be even higher than that for the catalyst treated at 400 °C. This suggests that Co oxide is very likely present in the thermally treated catalyst.

More quantitative structural information is obtained through fitting of the EXAFS data. Data and fits of the magnitude of Fourier transformed k^2-weighted EXAFS spectra at the Pt L_3 edge and the Ni K edge of $Pt_{64}Ni_{36}$/C catalyst are shown in Figure 6. Excellent fits are obtained for the first coordination shell around Ni and Pt. Structural parameters obtained from the fitting of EXAFS data at the Ni K edge and the Pt L3 edge are listed in Table 2. For Ni K edge spectra, best fits are achieved by including O, Ni, and Pt in the first shell. On the basis of the coordination number (N), which is a measure of the average number of a specific first-shell neighbor around the absorbing center (Ni or Pt), O is found to be present around Ni and Pt, confirming the existence of Ni oxide and Pt oxide. The EXAFS data also

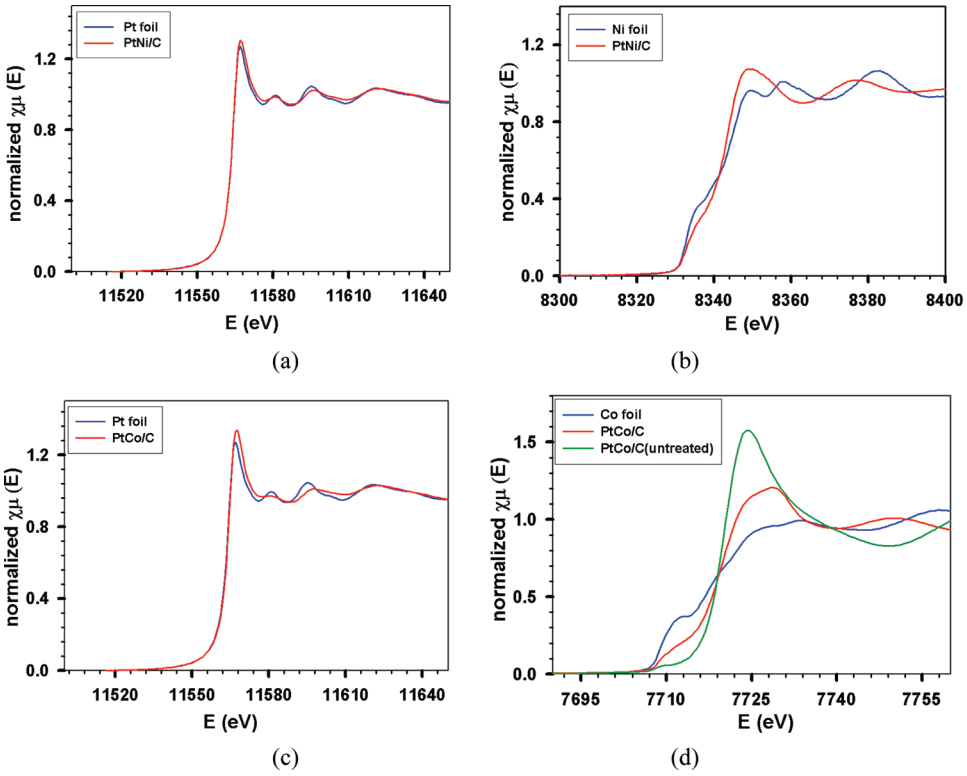

Figure 5. Normalized XANES spectra at the Pt L_3 edge (a) and Ni K edge (b) for $Pt_{64}Ni_{36}$/C treated at 400 °C and the Pt L_3 edge (c) and Co K edge (d) for $Pt_{52}Co_{48}$/C treated at 400 °C. Note that the green curve in (d) is for a sample of untreated $Pt_{52}Co_{48}$/C.

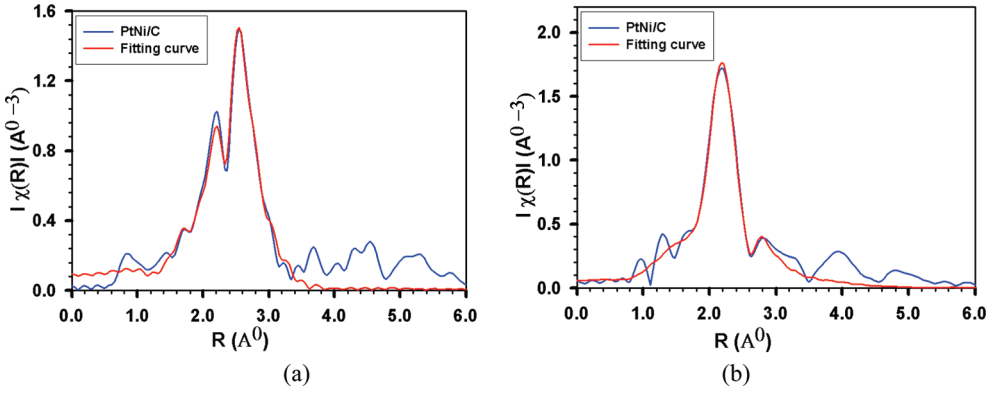

Figure 6. Data and fits of the magnitude of Fourier transformed k^2-weighted EXAFS spectra of $Pt_{64}Ni_{36}$/C catalyst at (a) the Pt L3 edge and (b) the Ni K edge.

Table 2. Structural Parameters Obtained from the Fitting of EXAFS Data at the Ni K Edge and the Pt L3 Edge for $Pt_{64}Ni_{36}$/C (8.7 ± 0.8 nm)

scatterer	*N*	*R* bond length (Å)	disorder (× 10^{-3} Å^2)
Pt−O	0.4 ± 0.1	2.02 ± 0.03	10.3 ± 9.4
Pt−Ni	1.0 ± 0.4	2.65[a]	9.9[a]
Pt−Pt	8.7 ± 0.7	2.74 ± 0.00	6.3 ± 0.4
Ni−O	0.8 ± 0.3	1.97 ± 0.02	10.3 ± 9.4
Ni−Ni	4.1 ± 0.5	2.51 ± 0.00	8.1 ± 1.1
Ni−Pt	3.5 ± 0.5	2.65 ± 0.01	9.9 ± 1.8

[a] Fixed at values obtained from fitting of Ni K edge EXAFS.

confirmed the formation of alloy by the identification of Pt as the first-shell neighbor around Ni and Ni as the first-shell neighbor around Pt. The observation of Ni in the first shell of Ni and Pt in the first shell of Pt can in general result from (1) Ni−Pt alloy or (2) segregated Ni phase or Pt phase (for example, small domains of Ni or Pt in the particle). The fitted Ni−Ni is 0.03 Å longer than that in Ni foil (fitted value of 2.48 Å), while the Pt−Pt bond distance is 0.02 Å shorter than that in Pt foil (fitted value of 2.76 Å).

From the O coordination number, it was estimated that the content of Pt in the oxide form is about 7% (i.e., 0.4/6), and that of Ni in the oxide form is 0.8/6 = 13%. This estimate was based on two assumptions: (1) surfaces of metal oxides are terminated by oxygen or hydroxyl, thus the metal in metal oxide is always fully coordinated; and (2) the metals are six-coordinated for Ni, Pt, or Co oxides. The first assumption is reasonable considering the facts that these thermally treated catalysts have been exposed to ambient conditions for an extensive period of time under which it is likely that the surface is covered by a monolayer of O

dx.doi.org/10.1021/jp109630n |*J. Phys. Chem. C* 2011, 115, 1682–1694

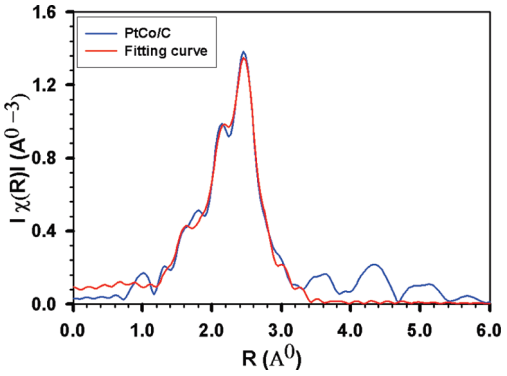

Figure 7. Data and fits of the magnitude of Fourier transformed k^2-weighted EXAFS spectra of the $Pt_{52}Co_{48}/C$ catalyst at the Pt L_3 edge.

Table 3. Structural Parameters Obtained from the Fitting of EXAFS Data at the Pt L3 Edge for $Pt_{52}Co_{48}/C$ (3.9 ± 0.7 nm)

scatterer	*N*	*R* bond length (Å)	disorder (× 10^{-3} Å^2)
Pt−O	0.6 ± 0.1	1.98 ± 0.02	4.0 ± 3.4
Pt−Co	2.8 ± 0.4	2.64 ± 0.01	8.6 ± 1.3
Pt−Pt	5.3 ± 0.6	2.70 ± 0.00	6.2 ± 0.5

or OH species. The second assumption is supported by some literature data known for NiO, CoO, and PtO_2.[52]

The Fourier transform (FT) EXAFS spectra for the Pt L_3 edge of the $Pt_{52}Co_{48}/C$ catalyst are shown in Figure 7, and the fitted parameters are listed in Table 3. In the fitting, O, Co, and Pt are included in the first shell. O is found to be present around Pt, confirming the existence of Pt oxide. From the O coordination number, it was estimated that the content of Pt in the oxide form is about 10% (i.e., 0.6/6). The EXAFS data also confirmed the formation of the Co−Pt alloy by the identification of Co as a first-shell neighbor around Pt. Unfortunately, the Co EXAFS data that we obtained were too noisy for producing a meaningful spectral fitting. The Co−Pt bond distance (2.65 Å) is very close to the Ni−Pt bond distance (2.64 Å), which can be expected from their atomic radii. What is surprising is the significant difference in Pt−Pt bond distance introduced by Ni and Co. Pt−Pt bond distance is 2.70 Å with Co and 2.74 Å with Ni. While the alloying effect is considered to be partially responsible for the shrinkage of the bond distance, the issue of how the particle size reduction contributes to bond distance reduction is yet to be investigated. In our previous studies of PtAu catalysts,[53,20] the reduction of the lattice constant as a result of the reduction of the particle size and alloying was supported by XRD data and DFT calculation results.

In summary, the XAFS data reveal the reduction of interatomic distances and the presence of metal oxides for both PtCo/C and PtNi/C catalysts. On the basis of the combined weight of the XRD data on alloying characteristics of these two catalysts and our XPS data on similar catalysts (e.g., PtNiCo/C catalysts[51]), the detected oxides are believed to be present largely on the surface. The Pt−Pt bond distance is found to be smaller for PtCo/C than for PtNi/C (Tables 2 and 3), which may be responsible for the higher activity shown by PtCo/C. The quantitative insights into the structural differences provide important information for assessing the difference in the relative amounts of PtO vs the base metal (M) oxides (CoO or NiO) and the relative change in bond distances of Pt−Pt vs Pt−M or M−M bonds in the bimetallic nanoparticle catalysts. The difference in Pt coordination number is apparently a result of the difference in particle sizes ($Pt_{64}Ni_{36}/C$ (8.7 nm) > $Pt_{52}Co_{48}/C$ (3.9 nm)). There are subtle differences in terms of the Pt−M and Pt−O coordination numbers. The coordination number for Pt−Co is clearly larger than that for Pt−Ni (by a factor of ∼3) (this conclusion is valid even by taking the composition difference into consideration where there is a 1.6-times higher Co % in PtCo than Ni % in PtNi), while the coordination number for Pt−O in PtCo is slightly larger than that for Pt−O in PtNi. The difference in Pt−M coordination number is believed to reflect partially the difference in the detailed structural characteristics in terms of the alloying vs phase segregation of these two bimetallic alloys. However, a further comparative EXAFS study with different particle sizes is needed for us to draw a clear conclusion on the size effect. This assessment is supported by the XAFS data indicating the presence of segregated phases in the PtNi nanoparticles. The slight increase in Pt−O coordination for PtCo vs PtNi could suggest an enhanced adsorption of oxygenated species on PtCo.

It is important to note that the EXAFS result is size dependent, and the result from the EXAFS study described in this report was discussed only in the context of metal−metal bonding changes, coordination number differences, and surface oxide formations for the as-prepared PtCo/C and PtNi/C catalysts, and any parallel comparison with the particle size effect cannot be drawn. These two catalysts were selected as they showed the highest activities among the tested PtCo/C and PtNi/C groups. They were used to illustrate the electrochemical characteristics, not to directly compare the ECA values. Although the EXAFS was performed ex situ, the data are reliable for assessing the structural characteristics of the as-prepared catalysts.

4. Electrocatalytic Activity for Oxygen Reduction Reaction. The carbon-supported multimetallic nanoparticle catalysts were examined using CV and RDE methods for assessing their electrocatalytic activity and stability for ORR. The catalysts were mixed with Nafion and iso-propanol in water to prepare the catalyst inks that were loaded on the glassy carbon electrode. The kinetic current from the RDE data provide quantitative measures for assessing the electrocatalytic activities in term of their correlation with the composition, size, and morphology. The electrochemical active area (ECA), mass activity (MA), and specific activity (SA) of the catalysts were determined from measurements of CV and RDE curves. Figure 8 shows a typical set of CV and RDE data for the PtCo/C and PtNi/C catalysts thermally treated at 400 °C.

For $Pt_{73}Co_{27}/C$ (2.8 ± 0.4 nm) and $Pt_{71}Ni_{29}/C$ (6.6 ± 1.0 nm) catalysts, the characteristics in the hydrogen adsorption/desorption region (Figure 8a and b) showed subtle differences. For $Pt_{73}Co_{27}/C$, an ECA value of 75 m^2/g_{Pt} was obtained. For $Pt_{71}Ni_{29}/C$, an ECA value of 27 m^2/g_{Pt} was obtained. In Table 4, ECA values were compared in terms of composition and particle sizes. The ECA values were found range from 40 to 75 m^2/g_{Pt} for different PtCo/C catalysts and from 24 to 55 m^2/g_{Pt} for different PtNi/C catalysts depending on size and composition.

A clear difference is also revealed in the kinetic region of the RDE curves (Figure 8c and d). The kinetic currents for these catalysts are translated to mass activity and specific activity to compare electrocatalytic activity (Table 4). Both the mass activity and specific activity data were obtained from the kinetic current at 0.858 V. In comparison, the electrochemical and electrocatalytic activity for the Pt/C catalyst from Etek (2.5 nm)

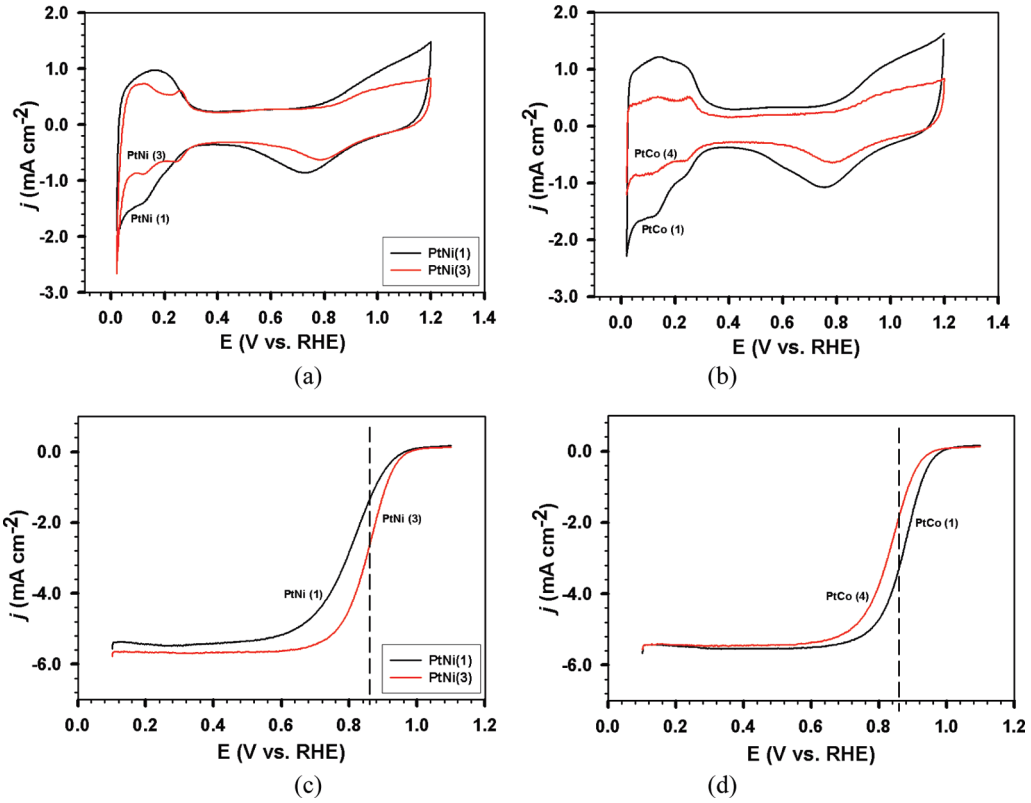

Figure 8. (a) and (b) are CV curves for PtNi(1), $Pt_{78}Ni_{22}$/C (2.7 ± 1.0 nm), and PtNi(3), $Pt_{71}Ni_{29}$/C (6.6 ± 1.0 nm), and PtCo(1), $Pt_{73}Co_{27}$/C (2.8 ± 0.4 nm), and PtCo(4), $Pt_{70}Co_{30}$/C (7.0 ± 0.7 nm), catalysts in 0.5 M H_2SO_4 in nitrogen-saturated solution. Scanning rate: 50 mV/s. (c) and (d) are the corresponding RDE curves in O_2-saturated 0.5 M H_2SO_4. Scanning rate: 5 mV/s. Catalyst amount: 15 μg. Electrode: 0.196 cm^2. Rotating speed: 2000 rpm. The vertical dash lines indicate the potential at which the kinetic current was analyzed (0.858 V).

Table 4. Summary of the Electrocatalytic Data for PtCo/C and PtNi/C Catalysts[a]

catalysts	particle size on carbon (nm)	metal loading (% wt)	lattice parameter (nm)	ECA (m^2/g_{Pt})	MA (A/mg_{Pt})	SA (mA/cm^2)
Pt/C_Etek	2.5 ± 0.5	20	-	91	0.22	0.24
Pt/C	7.1 ± 1.6	23	0.3947	55	0.11	0.20
(A) PtCo/C						
$Pt_{73}Co_{27}$/C	2.8 ± 0.4	37	0.3910	73	0.33	0.45
$Pt_{75}Co_{25}$/C	4.6 ± 0.6	40	0.3904	58	0.15	0.26
$Pt_{70}Co_{30}$/C	7.0 ± 0.7	36	0.3874	38	0.12	0.32
$Pt_{52}Co_{48}$/C	3.9 ± 0.7	24	0.3844	44	0.25	0.57
(B) PtNi/C						
$Pt_{71}Ni_{29}$/C	6.6 ± 1.0	45	0.3920	27	0.17	0.62
$Pt_{78}Ni_{22}$/C	2.7 ± 1.0	38	0.3895	55	0.07	0.13
$Pt_{64}Ni_{36}$/C	8.7 ± 0.8	24	0.3890	24	0.14	0.57
$Pt_{56}Ni_{44}$/C	6.1 ± 0.8	44	0.3817	25	0.17	0.69

[a] Catalyst: 15 μg. Electrode: 0.196 cm^2. Electrolyte: 0.5 M H_2SO_4. Scan rate: 5 mV/s. Rotating speed: 2000 rpm.

and Pt/C reported in our previous work (7.1 nm)[39] are also shown in Table 4.

For PtCo/C catalysts, the mass activity observed for the smaller sized samples was found to be higher than that of Pt/C. Note that the values of the mass activity are comparable with those reported previously for Pt_3Co_1 catalysts prepared differently.[23] In the previous report,[28,29] the mass activity was found to increase with particle size, reaching a maximum at around 4.5 nm. The catalysts with a smaller particle size were found to exhibit a higher activity than those with a larger size (e.g., $Pt_{73}Co_{27}$/C (2.8 ± 0.4 nm) > $Pt_{75}Co_{25}$ (4.6 ± 0.6 nm)). The catalysts with a higher Pt composition were found to exhibit a higher mass activity than those with a lower Pt composition (e.g., ($Pt_{73}Co_{27}$) > ($Pt_{52}Co_{48}$)) even when the size effect on the activity was considered for the two catalysts. It is clear that the activity is dependent not only on the synthesis and thermal treatment conditions but also on the particle size and composition. In the composition range reported in this manuscript, we found that the differences of mass activities for catalysts of specific composition with a variation in composition within a range of 5−10% might

dx.doi.org/10.1021/jp109630n |J. Phys. Chem. C 2011, 115, 1682–1694

be small in comparison with the size effect. Since the ECA, MA, and SA data were all normalized by the amount of Pt composition and the actual loading, the experimental results evidence that the mass activity difference was mainly from the particle size difference, not the composition and loading differences. It is important to emphasize that the comparison is confined within the tested composition and size ranges, and a more thorough investigation with a systematic change in size or composition for the catalysts is needed to fully assess the size and composition effects on the activity.

To make sure that the comparison of our electrochemical data was independent of electrolyte used, the PtCo/C and PtNi/C catalysts were also examined in different electrolytes. A representative set of ECA, MA, and SA data obtained from 0.5 M sulfuric acid to 0.1 M perchloric acid electrolytes are compared (see Supporting Information (Table S1)). There is no significant difference for data between these two electrolytes, validating the comparison of the data between these two electrolytes. The lack of a clear difference of the SA (or MA) data between sulfuric acid and perchloric acids (see Supporting Information Table S1) also suggests that the contribution of the possible adsorption of sulfate on (111) facets of larger-sized particles is unlikely to be significant under the experimental conditions.

In Figure 9A, the MA data were compared for PtCo/C and PtNi/C catalysts with different particle compositions and sizes for assessing the catalyst composition and size effects on the electrocatalytic activity. If the effect of the subtle differences in composition on the mass activity is assumed to be relatively less significant than the size effect which is supported by the experimental data and the base metal leaching is assumed to be the same for PtCo/C and PtNi/C, there appears to be a sharp contrast in terms of mass activity dependence on the particle size. While the mass activity shows a decrease with the increase in particle size for PtCo/C catalysts in the 3−8 nm range, it exhibits an increase with the particle size for the PtNi/C catalysts. Note that a similar trend was also observed for the specific activity for the PtNi/C catalysts, though it is less significant for the PtCo/C catalysts (Figure 9B). It is interesting to note that this trend is different from the size dependence of mass activity reported recently for Pt_3Co/C catalysts prepared by a different method,[27,28] which showed a maximum mass activity at 4.5 nm. In the previous work,[27,28] the size dependence was believed to reflect a balance of the average coordination number and the surface Co leaching of the catalysts and the enhanced adsorption of oxygenated species on the smaller sized particles, and consequently the decrease of the ORR activity, which was shown to be associated with the negative shift of the oxidation−reduction potential of surface Pt−O species with decreasing size.[27,28] As revealed in the study by Strasser et al.,[25] PtCo catalysts with a larger amount of oxygenated species, the surface Co oxides or subsurface species, were found to exhibit a relatively high specific activity. In our findings, while the exact origin for the mass activity decrease with increasing particle size is not identified at this time, the comparison between the size dependencies of the reduction potential of surface Pt−O species revealed a small negative shift for both PtCo/C and PtNi/C catalysts with the decrease in particle size. A close comparison of the potential shifts between PtCo/C and PtNi/C catalysts indicates that the potential for PtNi/C is slightly more negative (20−30 mV) than that for PtCo/C when the particle sizes are very small, whereas this difference diminishes when the particle sizes increase (see Supporting Information Table S2). While the marked difference in mass

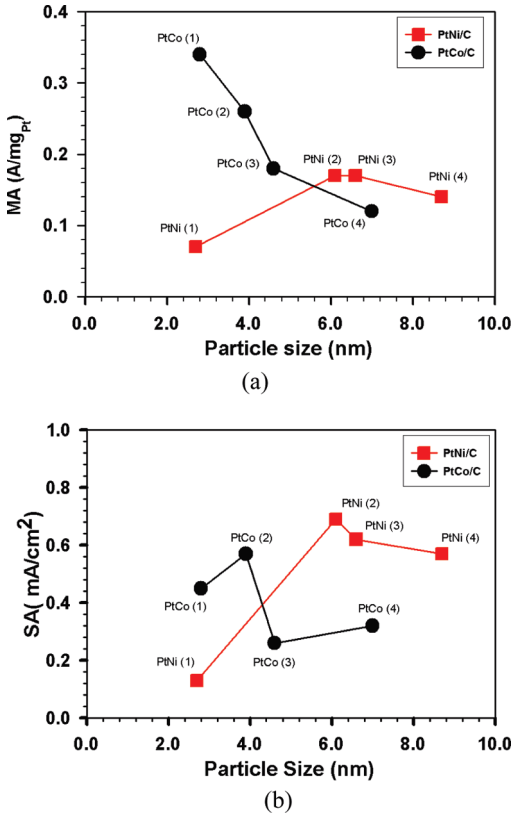

Figure 9. Comparison of mass activities (MA) (a) and specific activities (SA) (b) for a series of PtCo/C and PtNi/C catalysts. PtCo(1): $Pt_{73}Co_{27}$/C (2.8 ± 0.4 nm). PtCo(2): $Pt_{52}Co_{48}$/C (3.9 ± 0.7 nm). PtCo(3): $Pt_{75}Co_{25}$/C (4.6 ± 0.6 nm). PtCo(4): $Pt_{70}Co_{30}$/C (7.0 ± 0.7 nm). PtNi(1): $Pt_{78}Ni_{22}$/C (2.7 ± 1.0 nm). PtNi(2): $Pt_{56}Ni_{44}$/C (6.1 ± 0.8 nm). PtNi(3): $Pt_{71}Ni_{29}$/C (6.6 ± 1.0 nm). PtNi(4): $Pt_{64}Ni_{36}$/C (8.7 ± 0.8 nm).

activity observed for the smaller sizes and the small difference observed for the larger sizes (Figure 9A) seem to be associated with the size dependence of the potential shift, it can not be solely responsible for the size dependence of the activity because it can not explain the opposite size dependence of mass activity found for PtCo/C and PtNi/C catalysts and the higher mass activity of PtCo/C than PtNi/C in the size <5 nm range. On the basis of our XAS data, we believe that the smaller Pt−Pt bond distance for PtCo/C than for PtNi/C is partially responsible for the higher activity for PtCo/C. It is possible that the observed difference in size dependence of activity for these two bimetallic catalysts was in part due to the difference in the amount of surface oxygenated species between these two types of alloy nanoparticles, which could lead to the difference in electrocatalytic activity for ORR.[25,51] This assessment is supported by the XAFS-detected subtle differences in Pt−M (M = Ni and Co) bond distance and Pt−O coordination numbers, reflecting the presence of segregated phases in the PtNi nanoparticles and an enhanced adsorption of oxygenated species on PtCo nanoparticles, respectively. While these differences are believed to contribute to the observed differences in size dependence of the electrocatalytic activity, a more quantitative delineation of the ORR activity with the phase segregation and the surface oxygenated species is needed in further investigations of the different size bimetallic nanoparticle catalysts.

CONCLUSIONS

A size- and composition-controllable synthesis protocol was demonstrated for the preparation of PtCo and PtNi nanoparticles as electrocatalysts. By manipulating the relative concentrations of the metal precursors, the protocol produces PtCo and PtNi highly monodispersed nanoparticles with an average size in the range of 1.5−9.0 nm and controlled binary composition. The carbon-supported bimetallic alloy nanoparticles, after thermal treatment and calcination for effective removal of the capping molecules and alloying of the binary metals, were shown to exhibit enhanced electrocatalytic activities for ORR. The comparison between PtCo/C and PtNi/C catalysts revealed a sharp contrast in terms of size dependence of the activity. The mass activity showed a clear trend of decrease in activity with increasing particle size for PtCo/C catalysts, whereas it increases for PtNi/C catalysts. The detailed analyses of the structures of the catalysts by XAFS revealed important information for assessing the electrocatalytic properties in relation to the relative amount of oxygenated species and the relative change in interatomic bond distance in the bimetallic nanoparticles, which suggest that a combination of structural parameters such as Pt−Pt bond distance change, the segregation of metal phases, and the surface oxide formation are operative for the size dependence of the enhanced electrocatalytic activity. In addition to further structural correlation of the activity, a study of the stability of these catalysts in both electrochemical cells and fuel cells is also part of our ongoing work.

ASSOCIATED CONTENT

Supporting Information. Additional data of TEM, DCP−AES, and electrochemistry. This material is available free of charge via the Internet at http://pubs.acs.org.

AUTHOR INFORMATION

Corresponding Author

*E-mail: cjzhong@binghamton.edu.

Present Addresses

[||]ConocoPhillips, Research & Development, Bartlesville, OK 74004.

ACKNOWLEDGMENT

This work was supported by the National Science Foundation (CBET-0709113) and Honda. We also thank Dr. H. R. Naslund from the Department of Geology, SUNY-Binghamton, for assistance in DCP−AES analysis and Dr. I-T Bae, S3IP, Binghamton, for assistance in HR-TEM analysis. MRCAT operations are supported by the Department of Energy and the MRCAT member institutions.

REFERENCES

(1) Aiken, J. D., III; Finke, R. G. *J. Mol. Catal. A* **1999,** *145*, 1–44.
(2) Li, H.; Luk, Y. Y.; Mrksich, M. *Langmuir* **1999,** *15*, 4957–4959.
(3) Ingram, R. S.; Murray, R. W. *Langmuir* **1998,** *14*, 4115–4121.
(4) Zhong, C. J.; Luo, J.; Njoki, P. N.; Mott, D.; Wanjala, B.; Loukrakpam, R.; Lim, S.; Wang, L.; Fang, B.; Xu, Z. *Energy Environ. Sci.* **2008,** *1*, 454–466.
(5) Zhong, C. J.; Luo, J.; Fang, B.; Wanjala, B. N.; Njoki, P. N.; Loukrakpam, R.; Yin, J. *Nanotechnology* **2010,** *21*, 062001.
(6) Wasmus, S.; Kuever, A. *J. Electroanal. Chem.* **1999,** *461*, 14–31.
(7) Lipkowski, J.; Ross, P. N., Jr.; *Electrocatalysis, Frontiers in Electrochemistry*; VCH: New York, 1997; Vol. 5.
(8) Jarvi, T. D.; Sriramulu, S.; Stuve, E. M. *J. Phys. Chem. B* **1997,** *101*, 3649–3652.
(9) Tremiliosi, G.; Kim, H.; Chrzanowski, W.; Wieckowski, A.; Grzybowska, B.; Kulesza, P. *J. Electroanal. Chem.* **1999,** *467*, 143–156.
(10) Shukla, A. K.; Raman, R. K. *Annu. Rev. Mater. Res.* **2003,** *33*, 155–168.
(11) Adler, S. B. *Chem. Rev.* **2004,** *104*, 4791–4843.
(12) Hagelueken, C. PGM-Supply from Autocatalytic Recycling. *The Annual Precious Metals Seminar*, Toronto, November 15−16, 2001.
(13) Zhong, C. J.; Maye, M. M. *Adv. Mater.* **2001,** *13*, 1507–1511.
(14) Collman, J. P.; Bencosme, C. S.; Durand, R. R.; Kreh, R. P.; Anson, F. C. *J. Am. Chem. Soc.* **1983,** *105*, 2699–2703.
(15) Chu, D.; Jiang, R. *Solid State Ionics* **2002,** *148*, 591–599.
(16) Paulas, U. A.; Wokaun, A.; Scherer, G. G.; Schmidt, T. J.; Stamenkovic, V.; Radmilovic, V.; Markovic, N. M.; Ross, P. N. *J. Phys. Chem. B* **2002,** *106*, 4181–4191.
(17) Xiong, L.; Kannan, A. M.; Manthiram, A. *Electrochem. Commun.* **2002,** *4*, 898–903.
(18) Antolini, E.; Passos, R. R.; Ticianelli, E. A. *Electrochim. Acta* **2002,** *48*, 263–270.
(19) Lima, F. H. B.; Ticianelli, E. A. *Electrochim. Acta* **2004,** *49*, 4091–4099.
(20) Wanjala, B. N.; Luo, J.; Loukrakpam, R.; Mott, D.; Njoki, P. N.; Fang, B.; Engelhard, M.; Naslund, H. R.; Wu, J. K.; Wang, L.; Malis, O.; Zhong, C. J. *Chem. Mater.* **2010,** *22*, 4282–4294.
(21) He, T.; Kreidler, E.; Xiong, L. F. *J. Power Sources* **2007,** *165*, 87–91.
(22) He, T.; Kreidler, E.; Xiong, L. F.; Luo, J.; Zhong, C. J. *J. Electrochem. Soc.* **2006,** *153*, A1637–A1643.
(23) Chen, S.; Sheng, W. C.; Yabuuchi, N.; Ferreira, P. J.; Allard, L. F.; Shao-Horn, Y. *J. Phys. Chem. C* **2009,** *113*, 1109–1125.
(24) Koh, S.; Toney, M. F.; Strasser, P. *Electrochim. Acta* **2007,** *52*, 2765–2774.
(25) Koh, S.; Yu, C.; Mani, P.; Srivastava, R.; Strasser, P. *J. Power Sources* **2007,** *172*, 50–56.
(26) Schulenburg, H.; Muller, E.; Khelashvili, G.; Roser, T.; Bo"nnemann, H.; Wokaun, A.; Scherer, G. G. *J. Phys. Chem. C* **2009,** *113*, 4069–4077.
(27) Xu, Q.; Kreidler, E.; He, T. *Electrochim. Acta* **2010,** *55*, 7551–7557.
(28) Wang, C.; Van der Vliet, D.; Chang, K. C.; Markovic, N. M.; Stamenkovic, V. R. *Phys. Chem.* **2010,** *12*, 6933–6939.
(29) Wang, C.; Van der Vliet, D.; Chang, K. C.; You, H.; Strmcnik, D.; Schlueter, J. A.; Markovic, N. M.; Stamenkovic, V. R. *J. Phys. Chem. C* **2009,** *113*, 19365–19368.
(30) Qian, Y.; Wen, W.; Adcock, P. A.; Jiang, Z.; Hakim, N.; Saha, M. S.; Mukherjee, S. *J. Phys. Chem. C* **2008,** *112*, 1146–1157.
(31) Grinberg, V. A.; Kulova, T. L.; Maiorova, N. A.; Dobrokhotova, Zh. V.; Pasynskii, A. A.; Skundin, A. M.; Khazova, O. A. *Russ. J. Electrochem.* **2007,** *43*, 75–84.
(32) Zignani, S. C.; Antolini, E.; Gonzalez, E. R. *J. Power Sources* **2009,** *191*, 344–350.
(33) (a) Fowler, B.; Lucas, C. A.; Omer, A.; Wang, G.; Stamenkovic, V. R.; Markovic, N. M. *Electrochim. Acta* **2008,** *53*, 6076–6080. (b) Stamenkovic, V. R.; Fowler, B; Mun, B. S.; Wang, G. F.; Ross, P. N.; Lucas, C. A.; Markovic, N. M. *Science* **2007,** *315*, 493–497.
(34) Zhang, J.; Yang, H.; Fang, J.; Zou, S. *Nano Lett.* **2010,** *10*, 638–644.
(35) Wu, J.; Zhang, J.; Peng, Z.; Yang, S.; Wagner, F. T.; Yang, H. *J. Am. Chem. Soc.* **2010,** *132*, 4984–4985.
(36) Narayanan, R.; El-Sayed, M. A. *Top. Catal.* **2008,** *47*, 15–21.
(37) Chen, J.; Lim, B.; Lee., E. P.; Xia, Y. *Nanotoday* **2009,** *4*, 81–95.
(38) C. Wang, H.; Daimon, Y.; Lee, J.; Kim, S.; Sun, S. *J. Am. Chem. Soc.* **2007,** *129*, 6974–6975.
(39) Loukrakpam, R.; Chang, P.; Luo, J.; Fang, B.; Mott, D.; Bae, I.-T.; Naslund, H. R.; Engelhard, M. H.; Zhong, C. J. *Chem. Commun.* **2010,** *46*, 7184–7186.
(40) Greeley, J.; Norskov, J. K. *Electrochem. Acta* **2007,** *52*, 5829–5836.
(41) Greeley, J.; Norskov, J. K. *J. Phys. Chem. C* **2009,** *113*, 4932–4939.

(42) Ma, Y.; Balbuena, P. B. *J. Phys. Chem. C* **2008,** *112,* 14520–14528.
(43) Sun, S.; Murray, C. B.; Weller, D.; Folks, L.; Moser, A. *Science* **2000,** *287,* 1989–1992.
(44) (a) Luo, J.; Wang, L.; Mott, D.; Njoki, P. N.; Kariuki, N. N.; Zhong, C. J.; He, T. *J Mater. Chem.* **2006,** *16,* 1665–1673. (b) Luo, J.; Kariuki, N.; Han, L.; Wang, L.; Zhong, C. J.; He, T. *Electrochim. Acta* **2006,** *51,* 4821–4827. (c) He, T.; Kreidler, E.; Xiong, L.; Luo, J.; Zhong, C. J. *J. Electrochem. Soc.* **2006,** *153,* A1637–1643.
(45) Luo, J.; Han, L.; Kariuki, N.; Wang, L.; Mott., D.; Zhong, C. J.; He, T. *Chem. Mater.* **2005,** *17,* 5282.
(46) Chen, Y. S.; Fulton, J. L.; Partenheimer, W. J. *J. Solution Chem.* **2005,** *34,* 993–1007.
(47) Ravel, B.; Newville, M. *J. Synchrotron Radiat.* **2005,** *12,* 537–541.
(48) Newville, M. *J. Synchrotron Radiat.* **2001,** *8,* 322–324.
(49) Rehr, J. J.; Albers, R. C. *Rev. Mod. Phys.* **2000,** *72,* 621–654.
(50) Mukerjee, S.; McBreen, J. *J. Electrochem. Soc.* **1996,** *143* (7), 2285–2294.
(51) Wanjala, B. N.; Loukrakpam, R.; Lou, J.; Njoki, P. N.; Mott, D.; Zhong, C. J.; Shao, M.; Protsailo, L.; Kawamura, T. *J. Phys. Chem. C* **2010,** *114,* 17580–17590.
(52) Biswas, B.; Pieper, U.; Weyhermüller, T.; Chaudhuri, P. *Inorg. Chem.* **2009,** *48,* 6781–93.
(53) Luo, J.; Maye, M. M.; Petkov, V.; Kariuki, N. N.; Wang, L. Y.; Njoki, P.; Mott, D.; Lin, Y.; Zhong, C. J. *Chem. Mater.* **2005,** *17,* 3086–3091.